Embedded Active Sensors for In-Situ Structural Health Monitoring of Thin-Wall Structures

Victor Giurgiutiu
Mem. ASME
Associate Professor
e-mail: victorg@sc.edu

Andrei Zagrai
Graduate Research Assistant

JingJing Bao
Graduate Research Assistant

Department of Mechanical Engineering,
University of South Carolina,
Columbia, SC 29208

The use of embedded piezoelectric-wafer active-sensors for in-situ structural health monitoring of thin-wall structures is presented. Experiments performed on aircraft-grade metallic specimens of various complexities exemplified the detection procedures for near-field and far-field damage. For near-field damage detection, the electro-mechanical (E/M) impedance method was used. Systematic experiments conducted on statistical samples of incrementally damaged specimens were followed by illustrative experiments on realistic aging aircraft panels. For far-field damage detection, guided ultrasonic Lamb waves were utilized in conjunction with the pulse-echo technique. Systematic experiments conducted on aircraft-grade metallic plates were used to develop the method, while experiments performed on realistic aging-aircraft panels exemplified the crack detection procedure. [DOI: 10.1115/1.1484117]

Piezoelectric Active Sensors

Piezoelectric wafer active sensors (PWAS) offer new opportunities for developing embedded sensor arrays for in-situ structural health monitoring. These small, noninvasive, and inexpensive elastic wave generators/receptors can be easily affixed to the structure and intimately connected into interrogative sensor arrays [1]. Piezoelectric active sensors are nonresonant devices with wide band capabilities. They can be wired into sensor arrays that are connected to data concentrators and wireless communicators. Piezoelectric active sensors have captured the interest of the academic and industrial community due to their low cost and small nonintrusive nature [2–4].

The general constitutive equations of linear piezoelectric material behavior [5,6] describe a tensorial relation between mechanical and electrical variables (mechanical strain, S_{ij}, mechanical stress, T_{kl}, electrical field, E_k, and electrical displacement D_j) in the form

$$\begin{aligned} S_{ij} &= s^E_{ijkl} T_{kl} + d_{kij} E_k \\ D_j &= d_{jkl} T_{kl} + \varepsilon^T_{jk} E_k \end{aligned} \tag{1}$$

where s^E_{ijkl} is the mechanical compliance of the material measured at zero electric field ($E=0$), ε^T_{jk} is the dielectric permittivity measured at zero mechanical stress ($T=0$), and d_{kij} is the piezoelectric coupling between the electrical and mechanical variables. The *direct piezoelectric effect* is reflected in the second equation, while the first equation refers to the *converse piezoelectric effect*. In engineering notations, we write

$$\begin{Bmatrix} S_{11} \\ S_{22} \\ S_{33} \\ S_{23} \\ S_{31} \\ S_{12} \end{Bmatrix} \rightarrow \begin{Bmatrix} \varepsilon_{xx} \\ \varepsilon_{yy} \\ \varepsilon_{zz} \\ \varepsilon_{yz} \\ \varepsilon_{zx} \\ \varepsilon_{xy} \end{Bmatrix} \equiv \begin{Bmatrix} \varepsilon_1 \\ \varepsilon_2 \\ \varepsilon_3 \\ \varepsilon_4 \\ \varepsilon_5 \\ \varepsilon_6 \end{Bmatrix}, \quad \begin{Bmatrix} T_{11} \\ T_{22} \\ T_{33} \\ T_{23} \\ T_{31} \\ T_{12} \end{Bmatrix} \rightarrow \begin{Bmatrix} \sigma_{xx} \\ \sigma_{yy} \\ \sigma_{zz} \\ \sigma_{yz} \\ \sigma_{zx} \\ \sigma_{xy} \end{Bmatrix} \equiv \begin{Bmatrix} \sigma_1 \\ \sigma_2 \\ \sigma_3 \\ \sigma_4 \\ \sigma_5 \\ \sigma_6 \end{Bmatrix} \tag{2}$$

Hence, the constitutive equation (1) can be expressed, in matrix form, as

$$\begin{Bmatrix} \varepsilon_1 \\ \varepsilon_2 \\ \varepsilon_3 \\ \varepsilon_4 \\ \varepsilon_5 \\ \varepsilon_6 \end{Bmatrix} = \begin{bmatrix} s_{11} & s_{12} & s_{13} & & & \\ s_{21} & s_{22} & s_{23} & & & \\ s_{31} & s_{32} & s_{33} & & & \\ & & & s_{44} & & \\ & & & & s_{55} & \\ & & & & & s_{66} \end{bmatrix} \begin{Bmatrix} \sigma_1 \\ \sigma_2 \\ \sigma_3 \\ \sigma_4 \\ \sigma_5 \\ \sigma_6 \end{Bmatrix} + \begin{bmatrix} d_{11} & d_{12} & d_{13} \\ d_{21} & d_{22} & d_{23} \\ d_{31} & d_{32} & d_{33} \\ d_{41} & d_{42} & d_{43} \\ d_{51} & d_{52} & d_{53} \\ d_{61} & d_{62} & d_{63} \end{bmatrix} \begin{Bmatrix} E_1 \\ E_1 \\ E_1 \end{Bmatrix} \tag{3}$$

i.e.,

$$\{\boldsymbol{\varepsilon}\} = [\mathbf{s}]\{\boldsymbol{\sigma}\} + [\mathbf{d}]\{\mathbf{E}\} \tag{4}$$

For piezoelectric wafer active sensors, the mechanical stresses and strains are applied in the 1 and 2 directions, i.e., in the plane of the surface, while the electric field acts in the 3 direction, i.e., normal to the surface. Hence, the significant electro-mechanical couplings for this type of analysis are the 31 and 32 effects. The application of an electric field, E_3, induces surface strains, ε_1 and ε_2, and vice versa

$$\begin{aligned} \varepsilon_1 &= s_{11}\sigma_1 + s_{12}\sigma_2 + d_{13}E_3 \\ \varepsilon_2 &= s_{21}\sigma_1 + s_{22}\sigma_2 + d_{23}E_3 \end{aligned} \tag{5}$$

Figure 1(*a*) shows an active sensor consisting of a PZT (lead zirconate titanate oxide, $PbZr_xT_{1-x}O_3$) piezoceramic wafer affixed to the structural surface. As the PZT sensor is activated, interaction forces and moments appear (Fig. 1(*b*))

$$M_a = F_{\mathrm{PZT}}\frac{h}{2}, \quad F_{\mathrm{PZT}} = \hat{F}_{\mathrm{PZT}} e^{i\omega t}, \quad N_a = F_{\mathrm{PZT}} \tag{6}$$

Contributed by the Pressure Vessels and Piping Division and presented at the 7th Nondestructive Evaluation Topical Conference, San Antonio, Texas, April 23–25, 2001, of THE AMERICAN SOCIETY OF MECHANICAL ENGINEERS. Manuscript received by the PVP Division, May 4, 2001; revised manuscript received April 15, 2002. Associate Editor: S. Y. Zamrik.

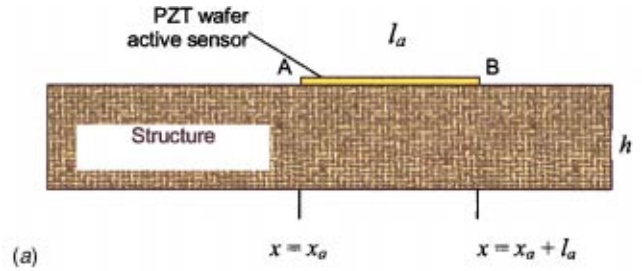

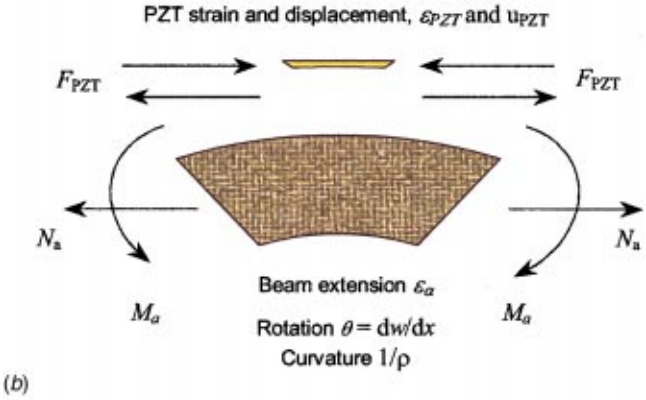

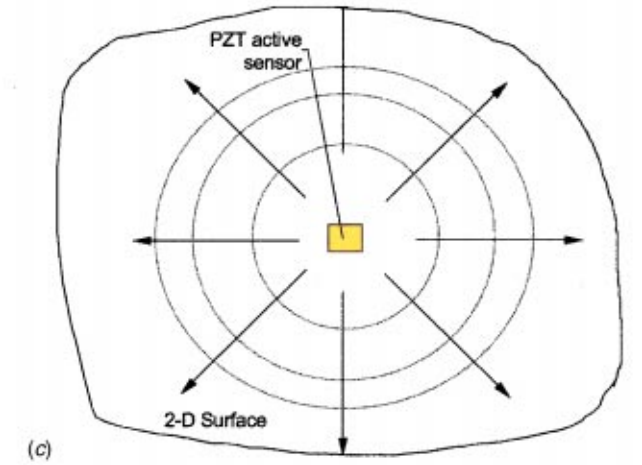

Fig. 1 Piezoelectric active sensor interaction with host structure: (*a*) PZT wafer affixed to the host structure; (*b*) interaction forces and moments; (*c*) active-sensor elastic waves interaction on a 2-D surface

If the active sensor is placed on a 2-D surface, the analysis is, in principle, two-dimensional (Fig. 1(*c*)). Since, for PZT, the electro-mechanical coupling constants, d_{31} and d_{32}, have essentially same value, radial symmetry can be applied, and the analysis can be reduced to 1-D in the radial coordinate, r [1].

Electro-Mechanical (E/M) Impedance Method

The structural impedance method is a damage detection technique complementary to the wave propagation techniques. Ultrasonic equipment manufacturers offer, as options, mechanical impedance analysis (MIA) probes and equipment [7]. The mechanical impedance method consists of exciting vibrations of bonded plates using a specialized transducer that simultaneously measures the applied normal force and the induced velocity. Cawley [8] extended Lange's work on the mechanical impedance method and studied the identification of local disbonds in bonded plates using a small shaker. Though phase information was not used in Cawley's analysis, present day MIA methodology uses both magnitude and phase information to detect damage.

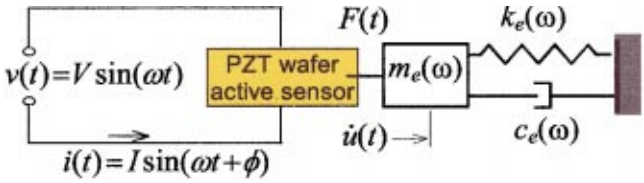

Fig. 2 Electro-mechanical coupling between the PZT active sensor and the structure

The electro-mechanical (E/M) impedance method is an emerging technology [9] that uses in-plane strain excitation at the structural surface to measure the pointwise mechanical impedance of the structure in the form of the real part of the electrical impedance at the sensor terminals. The principles of the E/M impedance technique are illustrated in Fig. 2. The effect of a piezoelectric active sensor affixed to the structure is to apply a local strain parallel to the surface that creates stationary elastic waves in the structure. The drive-point impedance presented by the structure to the active sensor can be expressed as a frequency-dependent quantity, $Z_{str}(\omega) = i\omega m_e(\omega) + c_e(\omega) - ik_e(\omega)/\omega$. Through the mechanical coupling between the PZT active sensor and the host structure, on one hand, and through the electro-mechanical transduction inside the PZT active sensor, on the other hand, the drive-point structural impedance gets expressed in the effective electrical impedance, $Z(\omega)$, as seen at the active sensor terminals

$$Z(\omega) = \frac{1}{i\omega \cdot C}\left[1 - \kappa_{31}^2\left(1 - \frac{1}{\varphi \cot \varphi + r(\omega)}\right)\right]^{-1} \tag{7}$$

where C is the zero-load capacitance of the PZT active sensor, κ_{31} is the electro-mechanical cross-coupling coefficient of the PZT active sensor ($\kappa_{31} = d_{13}/\sqrt{s_{11}\varepsilon_{33}}$), $r(\omega)$ is the impedance ratio between the pointwise structural impedance, $Z_{str}(\omega)$, and the impedance of the PZT active sensor, Z_{PZT}, and $\varphi = 1/2\gamma l_a$, with γ_a being the active sensor wave number and l_a its linear dimension. The electro-mechanical impedance method is applied by scanning a predetermined frequency range in the high kHz band and recording the complex impedance spectrum. By comparing the impedance spectra taken at various times during the service life of a structure, meaningful information can be extracted pertinent to structural degradation and the appearance of incipient damage. (It must be noted that the frequency range must be high enough for the signal wavelength to be significantly smaller than the defect size.)

Recent developments in E/M impedance structural health monitoring have focused on finding an effective damage metric to compare the E/M impedance spectra of pristine and damaged structures. Lopes et al. [10] used neural network techniques to process high-frequency E/M impedance spectra. Soh et al. [11] studied the performance of piezoelectric patches in health monitoring of a reinforced concrete bridge. Tseng et al. [12] studied nonparametric damage detection metrics based on various statistical quantities.

Calibration of E/M Impedance Method Through Systematic Circular-Plate Experiments. A series of systematic experiments were conducted on thin-gage aluminum plates to improve our understanding of the E/M impedance method and collect calibration data. Twenty-five circular-plate specimens (100 mm diameter, 1.6 mm thick) were constructed from aircraft-grade aluminum stock. Each plate was instrumented with one 7-mm-dia PZT active sensor placed at its center (Fig. 3). A 10-mm circumferential slit EDM was used to simulate crack-type damage. The crack was placed at increasing distance from the sensor (Fig. 3(*b*)). Thus, five statistical groups (Groups 0–4) were obtained. Each group was made up of five identical plates. E/M impedance

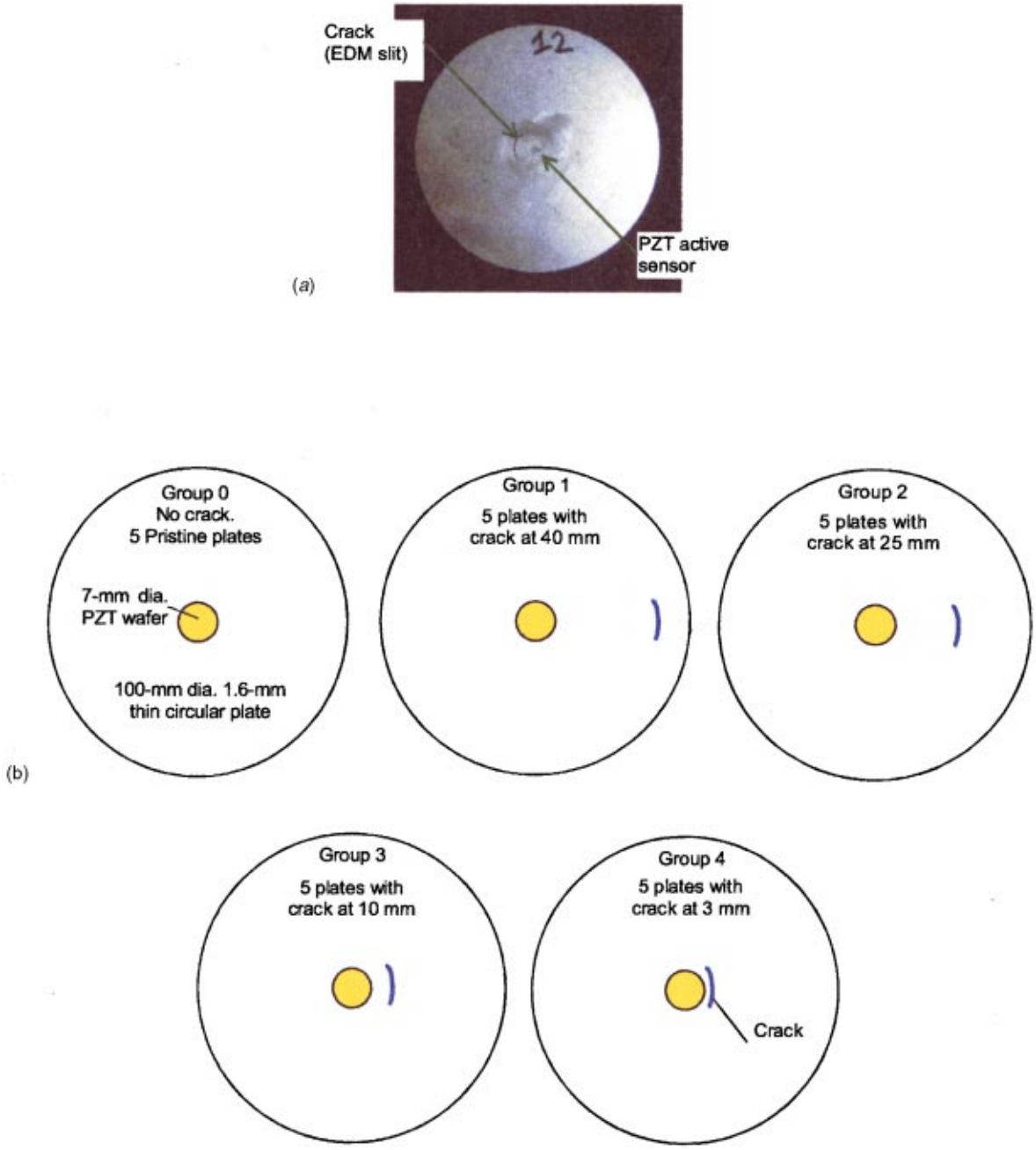

Fig. 3 Systematic study of E/M impedance technique on circular plates: (*a*) photograph of actual specimen showing a 7-mm active sensor of the sensor and a simulated crack (EDM slit); (*b*) progression of specimen geometries with simulated cracks (slits) at increasing distance from the E/M impedance sensor

data was taken using an HP 4194A impedance analyzer. During the experiments, the specimens were supported on packing foam to simulate free-free conditions.

The experiments were conducted over three frequency bands: 10–40 kHz, 10–150 kHz, and 300–450 kHz. The data were processed by displaying the real part of the E/M impedance spectrum, and determining a damage metric to quantify the difference between two spectra. Several damage metrics were tried: root mean square (RMS) deviation; mean absolute percentage deviation; covariance change; correlation coefficient (R^2) deviation. Figure 4 shows data in the 300–450 kHz band. The superposed spectra from specimens belonging to Groups 0 and 4 (extreme situations) are shown in Fig. 4(*a*), while those for Groups 0 and 1 (almost similar situations) are shown in Fig. 4(*b*). Figure 4(*a*) indicates that the presence of the crack in the close proximity of the sensor drastically modifies the point-wise frequency response function, and hence the real part of the E/M impedance spectrum. Resonant frequency shifts and the appearance of new resonances are noticed. In contrast, the presence of the crack in the far field only marginally modifies the frequency spectrum (Fig. 4(*b*)). Figure 4(*c*) presents the plot of the third power of the correlation coefficient deviation, $(1-R^2)^3$. It is clear from Fig. 4(*c*) that the $(1-R^2)^3$ damage metric decreases as the distance between the crack and the sensor increases. This experiment has shown, as expected, that:

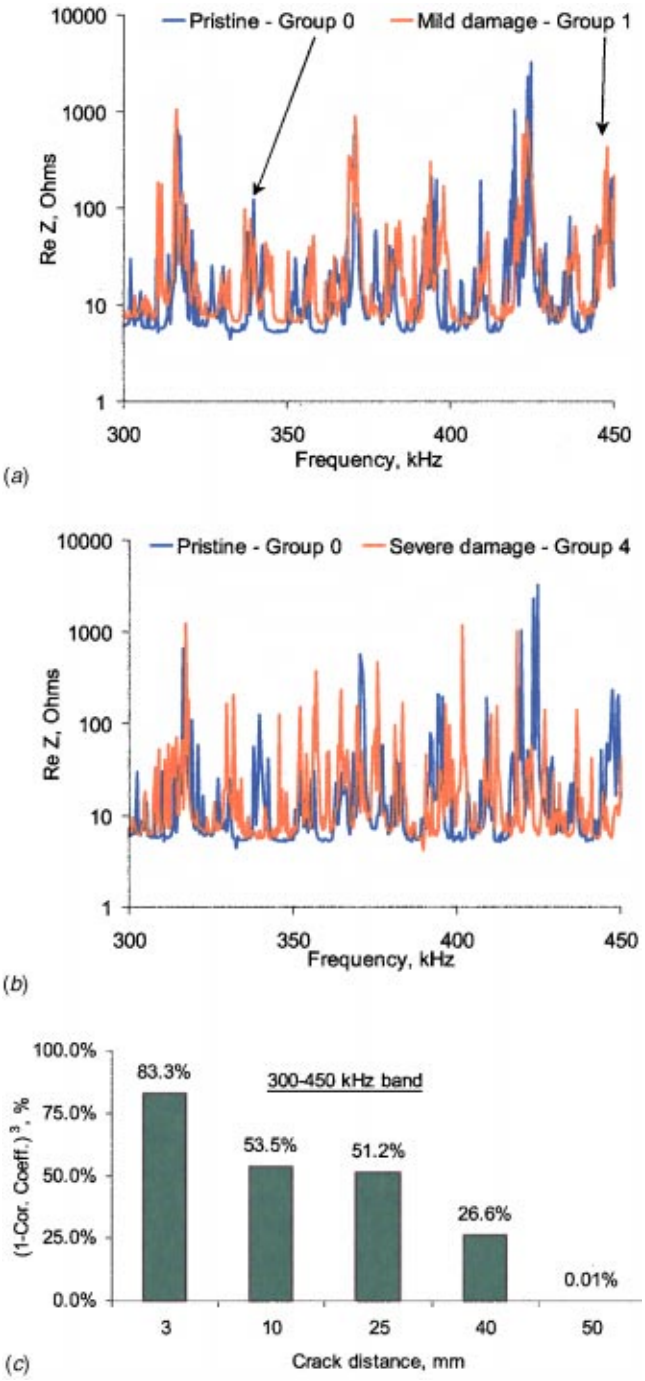

Fig. 4 E/M impedance results in the 300–450 kHz band: (*a*) mild damage effects on spectrum; (*b*) severe damage effects on spectrum; (*c*) damage metric variation with the distance between the crack and the sensor

(a) the crack presence in the near-field of the sensor drastically modifies the pointwise frequency response function, and hence the real part of the E/M impedance spectrum;
(b) this modification decreases as the distance between the sensor and the crack increases.

However, further work is needed to systematically investigate the most appropriate damage metric that can be used for processing the frequency spectra successfully under various damage situations.

E/M Impedance Experiments on Aging Aircraft Panels. Realistic aerospace panel specimens containing simulated crack and corrosion damage were designed and constructed at Sandia National Labs. These panels were instrumented with PZT active sensors and subjected to E/M impedance evaluation. The purpose of the experiment was to detect the change of E/M impedance spectrum induced by the presence of a simulated crack. Figure 5 shows the installation of the sensors: the sensors are placed along a line, perpendicular to a 10-mm crack originating at a rivet hole. The sensors are 7 mm square and are spaced at 7-mm pitch. E/M impedance readings were taken of each sensor in the 200–2600-kHz range. Figure 6(*a*) shows the frequency spectrum of the E/M impedance real part. The spectrum reflects clearly defined resonances that are indicative of the coupled dynamics between the PZT sensors and the frequency-dependent pointwise structural stiffness as seen at each sensor location. The spectrum presented in Fig. 6(*a*) shows high consistency. The dominant resonance peaks are consistently in the same frequency range and the variations from sensor to sensor are consistent with the variations previously recorded in the simple plate experiments.

Examination of Fig. 6(*a*) indicates that out of the four E/M impedance spectra, that of sensor 1 (closest to the crack) has lower frequency peaks, which could be correlated to the damage presence. However, this argument is not entirely self-evident since the spectra in Fig. 6(*a*) also show other sensor-to-sensor differences that are not necessarily related to the crack presence. In order to better understand these aspects, further investigations were performed at lower frequencies, in the 50–1000-kHz range (Fig. 6(*b*)). In this range, we can see that the crack presence generated features in the E/M impedance spectrum of sensor 1 (placed closest to the crack) that did not appear in the spectra of other sensors. For example, the sensor 1 spectrum presents an additional frequency peak at 114 kHz that is not present in the other sensors. It also shows a downward shift of the 400-kHz main peak. These features indicate a correlation between the particularities of sensor 1 spectrum and the fact that sensor 1 is placed closest to the crack. However, at this stage of the investigation, these correlations are not self-evident, nor are they supported by theoretical analysis and predictive modeling of the structure under consideration. Further signal processing and features extraction improvements are needed to fully understand the correlation between the spectral features of the E/M impedance response and the presence of structural damage in the sensor vicinity.

E/M Impedance Damage Detection Strategy. Based on the results presented in the previous section, we propose the following the damage-detection strategy to be used for near-field structural health monitoring using the E/M impedance method. The real part of the E/M impedance (Re *Z*) reflects the pointwise mechanical impedance of the structure, and the E/M impedance spectrum is equivalent to the pointwise frequency response of the structure. As damage develops in the structure in the form of cracks, corrosion, and disbonds, the pointwise impedance measured near the damage location changes. Piezoelectric active sensors placed at critical structural locations will be able to detect these near-field changes. In addition, due to the sensing localization property of this method, far-field influences will not be registered in the E/M impedance spectrum. The integrity of the sensor itself is independently confirmed using the imaginary part of E/M impedance (Im *Z*), which is highly sensitive to sensor disbond, but much less sensitive than the real part to structural resonances (Fig. 7).

To illustrate the proposed near-field damage detection strategy, consider an array of four active sensors as presented in Fig. 8. Each active sensor has its own sensing area resulting from the application of the localization concept. This sensing area is characterized by a sensing radius and the corresponding sensing circle. Inside the sensing area, the sensor detection capability decreases with the distance away from the sensor. A damage feature that is placed in the near field of the sensor is expected to create a dis-

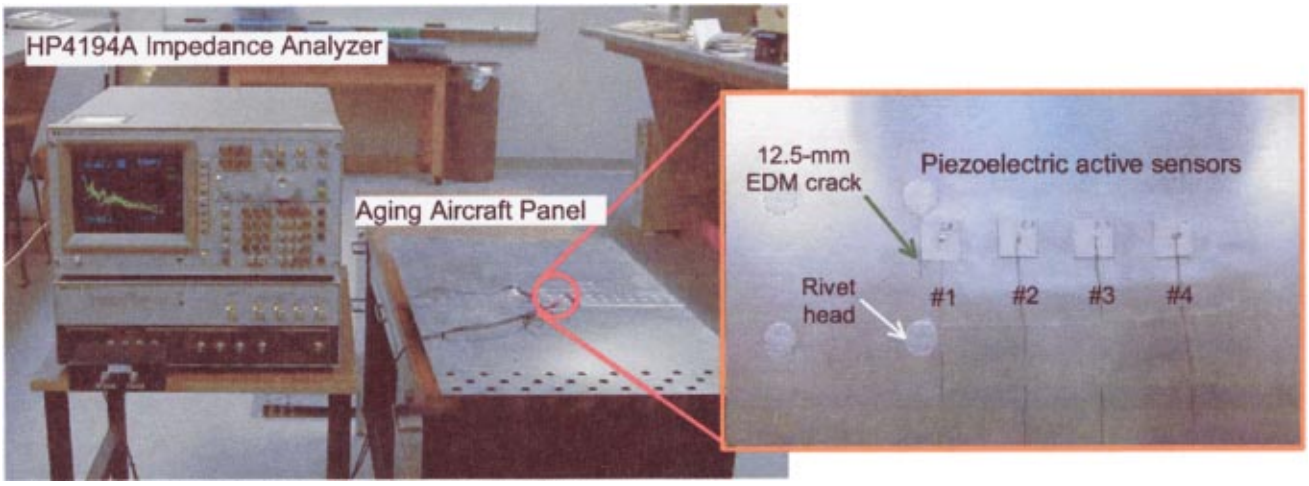

Fig. 5 The detection of simulated crack damage in aging aircraft panels using the E/M impedance method. Four rivet heads, four PZT active sensors, and a 10-mm EDM-ed notch (simulated crack) are featured

turbance in the sensor response that is larger than a damage feature placed in the far field. Effective area coverage is ensured when the sensing circles overlap. Structural cracks, corrosion, and disbonds/delaminations present in the sensor sensing area can be effectively detected (Fig. 8). The limitations of the E/M impedance method reside in its sensing localization, which diminishes its ability to detect far-field damage. For this latter case, the ultrasonic guided wave methods, discussed in the next section, may be more appropriate.

Guided Plate Waves (Lamb Waves) Method

Lamb waves (a.k.a., guided plate waves) are a type of ultrasonic waves that are guided inside thin plates [13]. Lamb waves can propagate in a number of modes, either symmetrical or antisymmetrical. The velocity depends on the product of frequency and material thickness. Investigations on Lamb and leaky Lamb waves have been carried out continuously since their discovery, and researchers have done theoretical and experimental work for different purposes, ranging from seismology, to ship construction industry, to acoustic microscopy, and to nondestructive testing and acoustic sensors [14–16]. Keilers and Chang [17] and Chang [18] used piezoelectric-wafers to detect damage-detection in composite plates. The Lamb wave speed is obtained by solving the Rayleigh-Lamb equation. First, define $\xi = \sqrt{c_S^2/c_P^2}$, $\zeta = \sqrt{c_S^2/c_L^2}$, and $d = k_S d$; where c_L is the Lamb wave speed, and d is the half-thickness of the plate. In addition, define Lamb wave number k_L

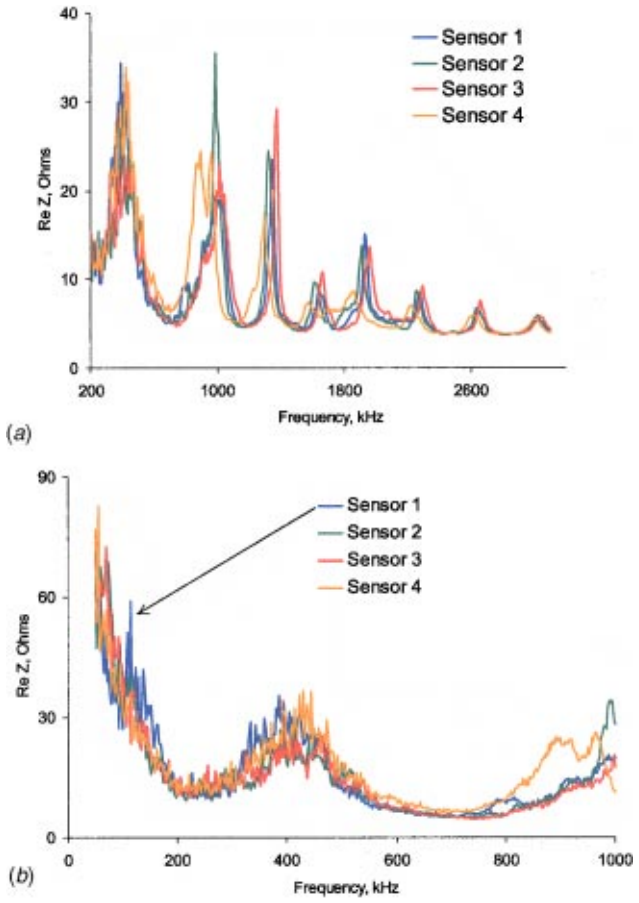

Fig. 6 Real part of impedance for sensors bonded on aging aircraft structure: (*a*) 200–2600-kHz range; (*b*) zoom into the 50–1000-kHz range

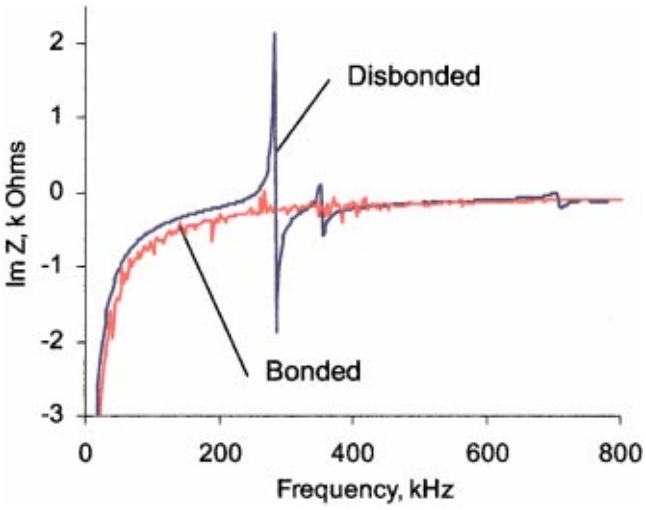

Fig. 7 Active sensor self-diagnostic using the imaginary part of the E/M impedance: when sensor is disbonded, new free-vibration resonance features appear at ~267 kHz (after [1])

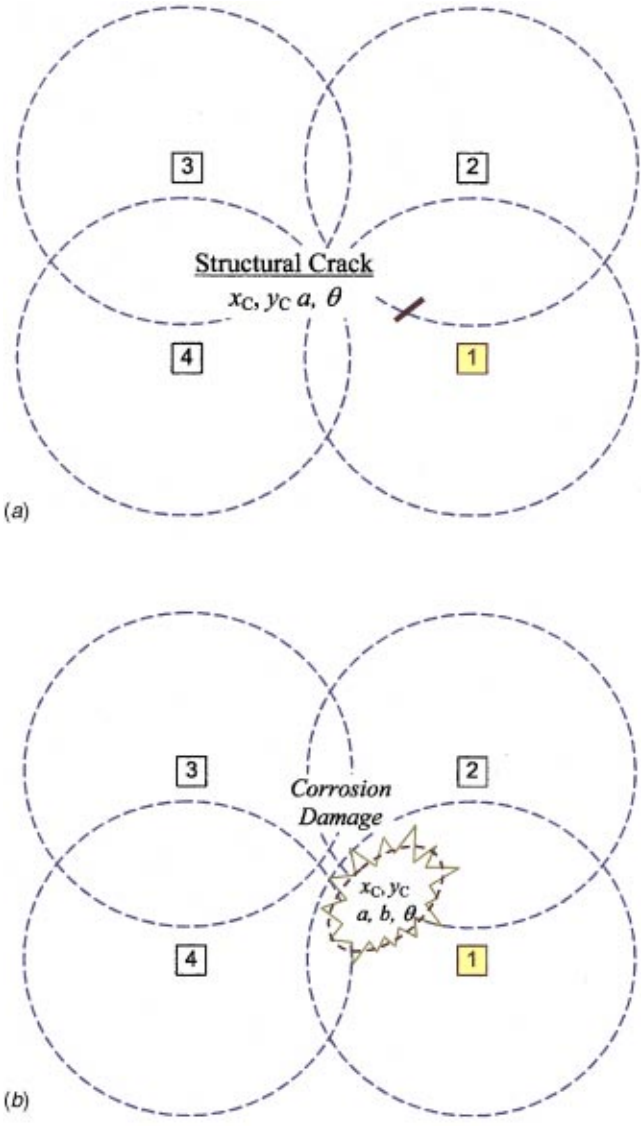

Fig. 8 Damage detection strategy using an array of 4 piezoelectric active sensors and E/M impedance method: (*a*) detection of structural cracks; (*b*) detection of corrosion damage. The circles represent the sensing radius of each active sensor.

$=\omega/c_L$, and the variables, $q=\sqrt{k_L^2-k_P^2}$, $s=\sqrt{k_L^2-k_S^2}$. Then, for symmetric wave motion (Fig. 9(*a*)), the Rayleigh-Lamb frequency equation can be written as

$$\frac{\tan(\sqrt{1-\zeta^2}\overline{d})}{\tan\sqrt{\xi^2-\zeta^2}}+\frac{4\zeta^2\sqrt{1-\zeta^2}\sqrt{\xi^2-\zeta^2}}{(2\zeta^2-1)^2}=0 \tag{8}$$

Then one can write the two components of the particle movement as

$$U(x,z,t)=\mathrm{Re}\left[Ak_L\left(\frac{\cosh(qz)}{\sinh(qd)}-\frac{2qs}{k_L^2+s^2}\frac{\cosh(sz)}{\sinh(sd)}\right)e^{i(k_Lx-\omega t(\pi/2))}\right] \tag{9}$$

$$W(x,z,t)=\mathrm{Re}\left[Aq\left(\frac{\sinh(qz)}{\sinh(qd)}-\frac{2k_L^2}{k_L^2+s^2}\frac{\sinh(sz)}{\sinh(sd)}\right)e^{i(k_Lx-\omega t)}\right] \tag{10}$$

For antisymmetric motion (Fig. 9(*b*)), the Rayleigh-Lamb frequency equation is

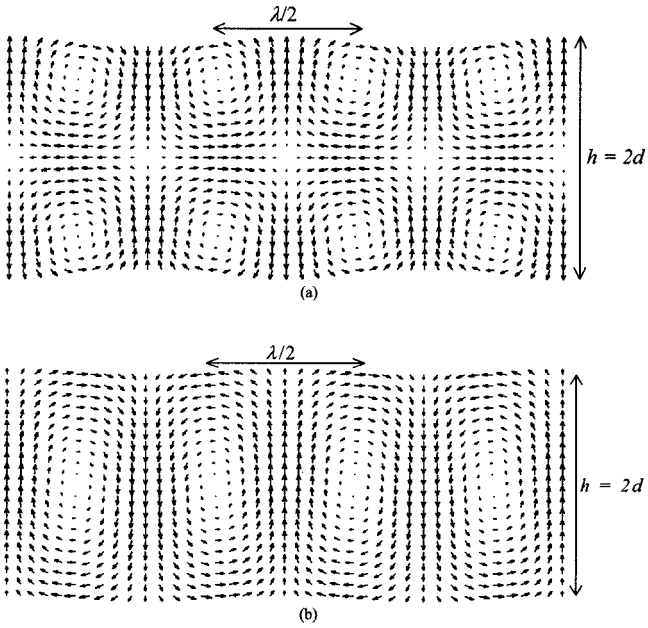

Fig. 9 Simulation of Lamb waves in a 1-mm thick aluminum plate: (*a*) symmetric mode S_0, $f=1.56$ MHz; (*b*) antisymmetric mode A_0, $f=0.788$ MHz. (For full animation, see http://www.engr.sc.edu/research/lamss/default.htm under research Thrust 1.)

$$\frac{\tan(\sqrt{1-\zeta^2}\overline{d})}{\tan\sqrt{\xi^2-\zeta^2}}+\frac{(2\zeta^2-1)^2}{4\zeta^2\sqrt{1-\zeta^2}\sqrt{\xi^2-\zeta^2}}=0 \tag{11}$$

The two components of the particle movement can be expressed as

$$U(x,z,t)=\mathrm{Re}\left[Ak_L\left(\frac{\cosh(qz)}{\cosh(qd)}-\frac{2qs}{k_L^2+s^2}\frac{\cosh(sz)}{\cosh(sd)}\right)e^{i(k_Lx-\omega t(\pi/2))}\right] \tag{12}$$

$$W(x,z,t)=\mathrm{Re}\left[Aq\left(\frac{\sinh(qz)}{\cosh(qd)}-\frac{2k_L^2}{k_L^2+s^2}\frac{\sinh(sz)}{\cosh(sd)}\right)e^{i(k_Lx-\omega t)}\right] \tag{13}$$

Figure 10 presents the dispersive (frequency-dependent) symmetric and antisymmetric (S_0 and A_0) Lamb wave speeds in 1.6-mm-thick aluminum plates.

The Need for High-Frequency Waves. In using guided waves to detect ultrasonic damage, two important aspects must be considered: (a) time resolution, and (b) defect size (detectable feature). The time resolution is especially important when using the pulse-echo method. Figure 11 shows guided Lamb waves traveling over a 800-mm length, first at 300 kHz (Fig. 11(*a*)), then at 20 kHz (Fig. 11(*b*)). At 300 kHz, the time resolution is sufficient since there is a signal free zone that makes it possible to easily establish the time of flight and detect reflected waves, if present. We also note that, at this high frequency, the S_0 wave becomes quickly fully established. At 20 kHz, the time resolution is insufficient, since the signal-free zone is too short and the wave is not yet fully established by the time the 800-mm length has been covered. At this low frequency, both A_0 and S_0 waves are excited. The S_0 wave travels faster, but with weaker amplitude. For illustration, Fig. 11(*b*) also presents waves detected at intermediate locations, i.e., 200, 400, and 600 mm.

High-frequency waves are also needed when detectable defect size must be considered. Figure 12 shows how the wavelengths of S_0 and A_0 Lamb waves vary with frequency. It is apparent that, in order to detect small size defects, high-frequency waves are re-

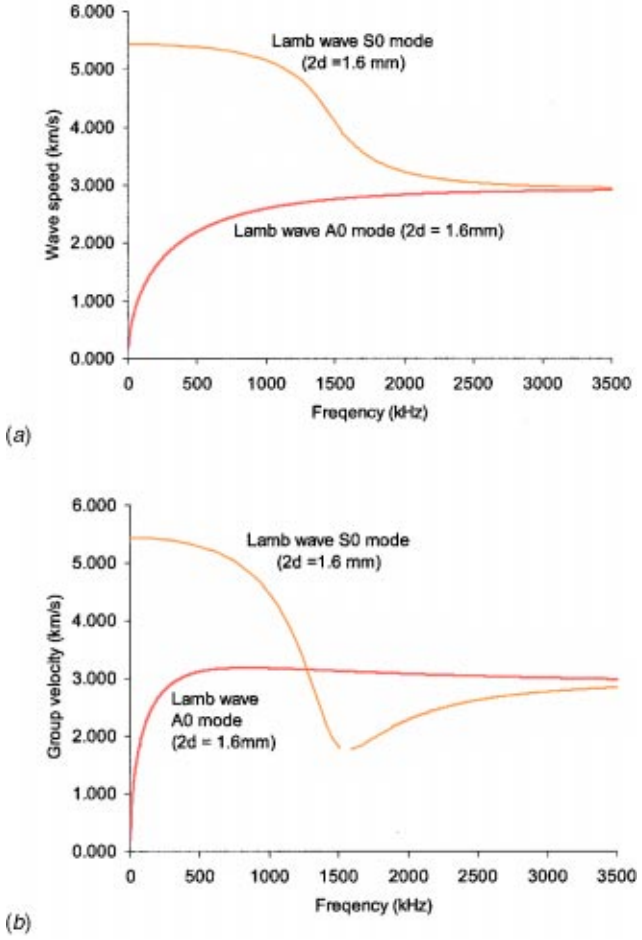

Fig. 10 Dispersion curves for S_0 and A_0 Lamb wave modes in thin-gage aluminum alloy structures: (*a*) wave speed, (*b*) group velocity

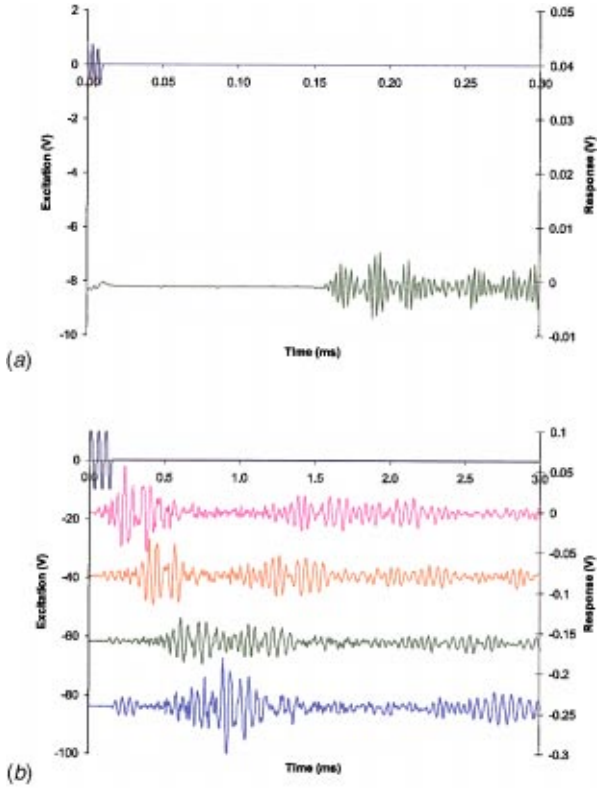

Fig. 11 Illustration of time resolution concept: (*a*) adequate time resolution at 300 kHz allows for clear delineation between transmitted and received waves; (*b*) inadequate time resolution at 20 kHz produces reception of arriving waves before generation of the transmitted wave being terminated

quired. Low-frequency Lamb waves can be used if the specimen length scale is large [19]. However, when the length scale of the specimen and/or defect size and location are small, high-frequency Lamb waves are required.

High-Frequency Lamb Wave Experiments on Rectangular Plates. Thin aluminum plate specimens were constructed from 1.6-mm-thick 2024-alloy stock in the form of a narrow strip (914 mm×14 mm×1.6 mm) and a rectangular plate (914 mm×504 mm×1.6 mm). The specimens were instrumented with arrays of 7-mm square PZT-wafer active sensors. The (x,y) sensor locations are given in Tables 1 and 2. The sensors were connected with thin insulated wires to a 16-channel signal bus and two 8-pin connectors (Fig. 13). An HP33120A arbitrary signal generator was used to generate a 300-kHz windowed harmonic-burst excitation to active sensor No. 11 with a 10-Hz repetition rate. Under harmonic burst excitation, the active sensor generates a package of elastic waves that spread out into the entire plate according to a circular wave front pattern. A Tektronix TDS210 two-channel digital oscilloscope, synchronized with the signal generator, was used to collect the response signals from the active sensors. The two oscilloscope channels were digitally switched among the remaining 10 active sensors using a digitally controlled switching unit. A LabView data acquisition program was developed to control the signal switch and record the data from the digital oscilloscope. In addition, a Motorola MC68HC11 microcontroller was tested as an embedded stand-alone controlling option.

The results for the narrow strip specimens were encouraging, but not perfect. They showed acceptable correlation between the

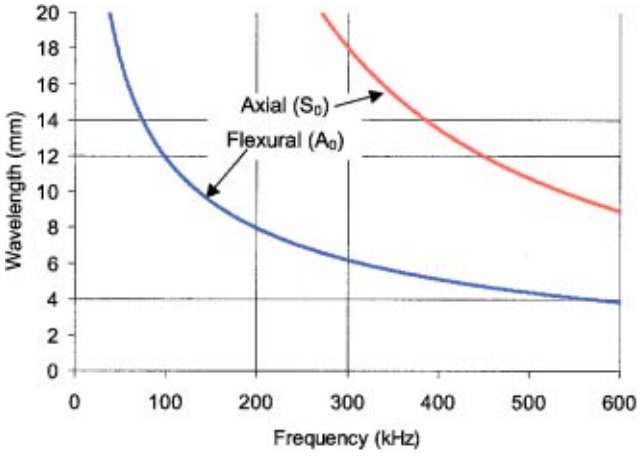

Fig. 12 Wavelength-frequency correlation for Lamb waves in 1.6-mm aluminum alloy plate

Table 1 Locations of sensors on the thin narrow strip specimen

Sensor #	A	B	C	D	E
x (mm)	57	257	457	657	857
y (mm)	7	7	7	7	7

Table 2 Locations of sensors on the thin rectangular plate specimen

Sensor #	1	2	3	4	5	6	7	8	9	10	11
x (mm)	100	100	100	100	100	450	450	450	800	800	800
y (mm)	100	175	250	325	400	100	250	400	100	250	400

Table 3 Elastic wave reception data on the thin rectangular plate specimen

Sensor #	*x* (mm)	*y* (mm)	*r* (mm)	*t* (μs)
1	70	0	70.0	221
2	84	0	84.0	263
3	98	0	98.0	302
4	112	0	112.0	357
5	200	0	200.0	537
6	200	96	221.8	602

time of flight, distance, and group velocity, but the dispersion of the wave packets was much stronger than expected, even with a smoothed-windowed tone burst excitation. In contrast, the results for the rectangular plate were remarkably clear and easy to interpret. This discrepancy can be explained by the multiple reflections that occurred at the edges of the narrow strip specimen, interfered with the main waves, and produced confusing results. No such effects occurred in the rectangular plate because the edges were far away from the source. Hence, it was concluded that the narrow strip specimen, though easier and less expensive to construct, was merely a ''stepping-stone'' in our investigation and did not warren further attention.

A sample of the signals measured on the rectangular plate specimen is given in Fig. 14(*a*). The first row shows signal associated with sensor 11 (the transmitter). The ''initial bang'' generated by this active sensor, as well as a number of wave packages received on the same sensor in the pulse-echo mode, are present. The wave packages are reflections from the plate edges, and their time-of-flight (TOF) position is consistent with the distance from the sensor to the respective edges. The other rows of signals correspond to the receptor active sensors 1 through 8. Their TOF position is consistent with the distance between the transmitting and receiving active sensors. The consistency of the wave patterns is remarkable.

These raw signals were processed using a narrow-band signal correlation algorithm, which was followed by an envelope-detection method. As a result, the exact TOF for each wave package could be precisely identified (Table 3). When the TOF was plotted against radial distance between the receiving active sensor and the transmitting active sensor, a remarkably good straight line fit (99.99% R^2 correlation) was obtained (Fig. 14(*b*)). The slope of this straight line is the wave speed, 5.461 km/s. For the 1-6-mm aluminum alloy used in this experiment, the theoretical group velocity for S_0 mode is 5.440 km/s (Fig. 10(*b*)). The speed detection accuracy (0.3% error) is remarkable. Further systematic investigations were able to reproduce with good accuracy the

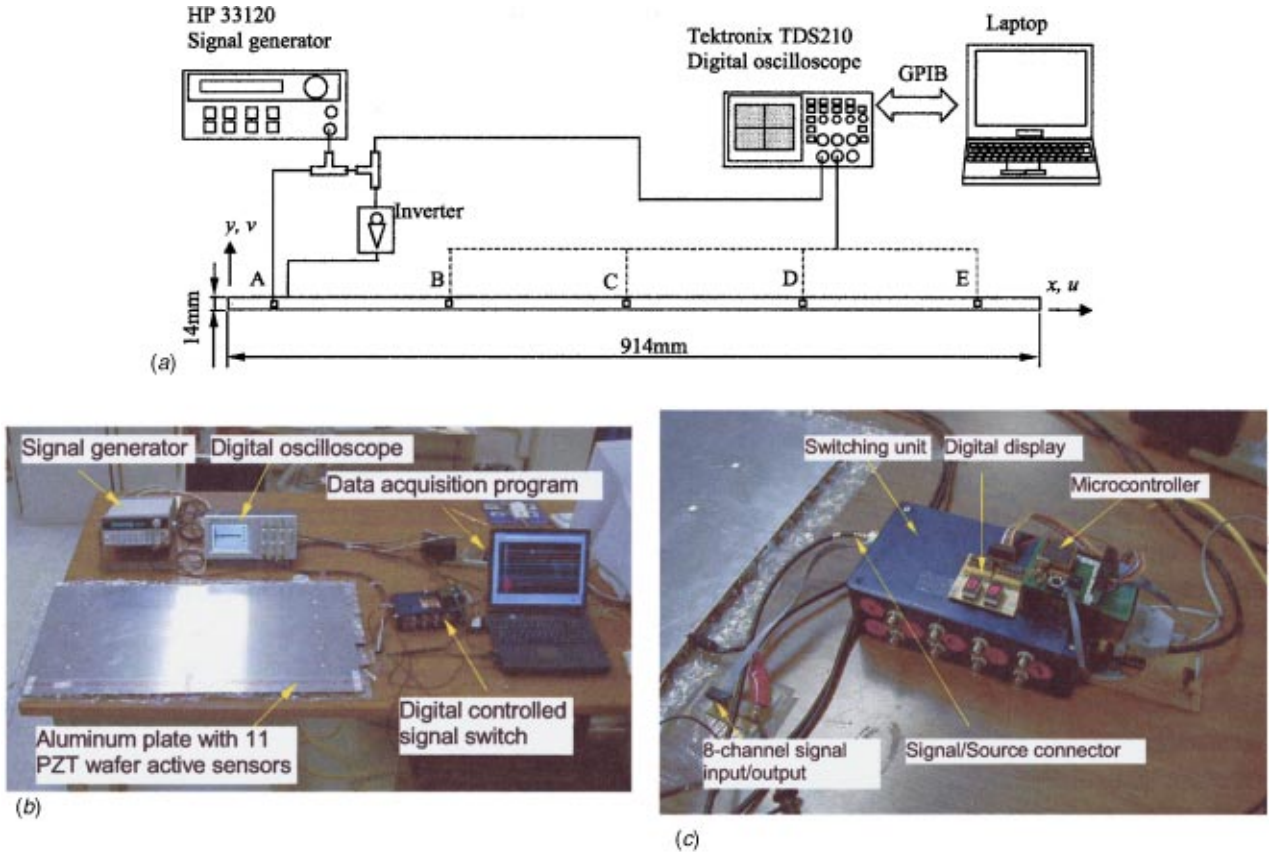

Fig. 13 Experimental setup for 2024 aluminum alloy, 1.6 mm thick, rectangular-plate wave propagation experiments: (*a*) schematic of the narrow strip (914 mm×14 mm×1.6 mm), active sensors, and instrumentation; (*b*) photograph of the rectangular plate (914 mm×504 mm×1.6 mm), active sensors, and instrumentation; (*c*) detail of the microcontroller switch box

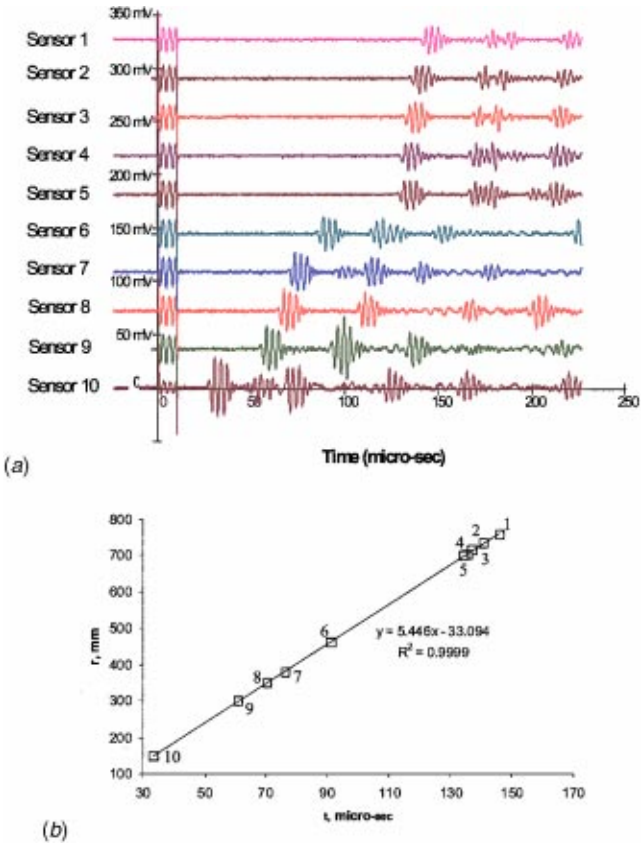

Fig. 14 (*a*) **Excitation signal and echo signals on active sensor 11, and reception signals on active sensors 1 through 8;** (*b*) **correlation between radial distance and time of flight**

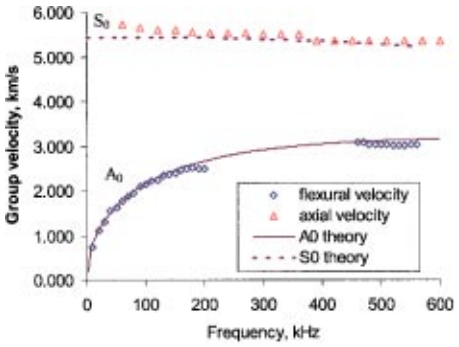

Fig. 15 Group velocity dispersion curves for Lamb wave A_0 and S_0 modes (measurements versus theory)

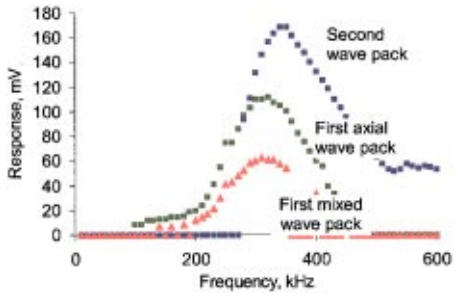

Fig. 16 Frequency tuning studies identified a maximum wave response around 300 kHz

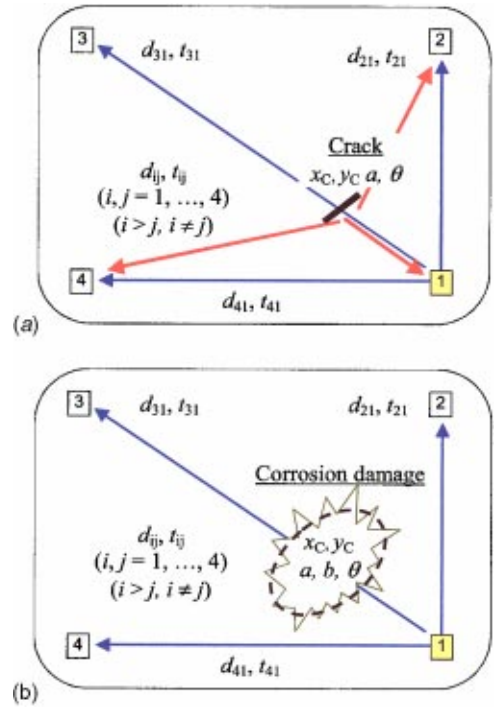

Fig. 17 Damage detection strategy using an array of four piezoelectric active sensors and wave propagation techniques: (*a*) **detection of structural cracks,** (*b*) **detection of corrosion damage**

group-velocity dispersion curves for the axial (S_0) and flexural (A_0) modes (Fig. 15), and to identify optimal excitation frequencies (Fig. 16).

Wave propagation damage detection experiments were conducted on realistic aircraft panel specimens with a number of PZT active sensors affixed at various locations. The experimental setup was similar to that used for the wave propagation calibration experiments on simple geometry specimens (Fig. 13). Several experiments were performed to verify the wave propagation properties, and to identify the reflections due to the construction features of the panels (rivets, splice joints, etc.) Then, damage detection strategies were developed.

Damage Detection Strategy With Guided Lamb Wave Method. The damage detection strategies using small nonintrusive active sensors and guided Lamb waves stem from ultrasonic and acousto-ultrasonic damage-detection methodology [20,21], respectively. Consider an array of four active sensors as presented in Fig. 17. Since piezoelectric active sensors can act as both sensors and actuators, our strategy assumes that one active sensor acts as actuator (1) while the others act as sensors (2, 3, and 4). Active sensor 1 generates elastic waves that propagate through the material and are sensed at active sensors 2, 3, and 4. To maximize the amount of data and mitigate experimental error, a round-robin process is applied, whereby active sensors 2, 3, and 4 in turn take the function of wave generators, with the rest of the active sensors being wave receptors. This method can be applied to detect two types of damage: cracks and corrosion.

Wave Propagation Detection of Structural Cracks. Crack damage is characterized in terms of its location, (x_C, y_C), and its size, a, and orientation θ. When a crack is present in the wave path, wave deflection/scatter, reflection, and transmission at the crack is expected (Fig. 17(*a*)). The proportion between deflection, reflection, and transmission will vary with damage size and orientation. In Fig. 17(*a*), active sensors 2 and 4 are shown to receive both direct and deflected waves. Active sensor 1 (the wave gen-

erator) also acts as a receptor and detects a reflected wave (echo). Active sensor 3 will receive a transmitted wave having its amplitude a function of damage size. Thus, a matrix of valuable information in terms of event arrival time can be set up. Mathematical solution will yield the damage location, size and orientation (x_C, y_C, a, θ). In the solution algorithm, conventional linear algebra solution methods and/or neural network algorithms can be employed.

Wave Propagation Detection of Corrosion Damage. Unlike crack damage, which is 1-dimensional, corrosion damage is 2-dimensional and can cover a wide area. In Fig. 17(*b*), active sensor 1 generates elastic waves that propagate through the material and are sensed at active sensors 2, 3, and 4. The waves will propagate differently through damaged material than through the pristine material. The difference will be in wave speed and attenuation. The corrosion damage has to be characterized in terms of its location, (x_C, y_C) and its size and orientation (a, b, θ, i.e., the major and minor axes of a damage ellipse, and axis inclination). In Fig. 17(*b*), the waves received by the active sensors 2 and 4 are shown to travel through pristine material, and hence will not be affected. The waves received by active sensor 3 travel through damaged material, hence a modification in their travel time (wave speed) and attenuation is expected. (If damage is very intense, the material degradation may be very advanced, and it is possible that no waves are received at active sensor 3.) Mathematical solutions, linear algebra or neural networks, yield the damage location, size and orientation (x_C, y_C, a, b, θ).

Summary and Conclusions

The aging of aerospace structures is a major current concern of civilian and military aircraft operators. Piezoelectric active sensors offer special opportunities for developing sensor arrays for in-situ health monitoring of aging aircraft fleet, because they are small, noninvasive, inexpensive, and easily wired into sensor arrays. This paper presents work done on developing and utilizing piezoelectric active sensor arrays to detect near-field and far-field damage in aircraft-grade metallic plates as well as in realistic built-up panels representative of aging aircraft structures. Damage due to structural cracks and corrosion was considered. For near-field damage detection, the electro-mechanical (E/M) impedance method was used. Systematic experiments conducted on statistical samples of incrementally damaged specimens were used to fully understand and calibrate this investigative method. Subsequent E/M impedance experiments were performed on realistic aging aircraft panels. The effect of simulated damage (12.5-mm crack) was noticed as a left shift in the natural frequencies for the sensor closest to the crack, and the appearance of a new frequency peak at around 114 kHz. However, complete understanding of the relationship between the sensor location and the changes in the E/M spectrum has not yet been fully achieved. Further efforts to refine the automatic detection and identification of the E/M impedance spectrum features that are sensitive to the crack presence are needed.

For far-field damage detection, ultrasonic techniques using guided Lamb wave were used. The need for high-frequency wave propagation to achieve the necessary time and space resolution in the given structural damage detection conditions was articulated and exemplified. A complete active-sensor array was installed and transmitter-receiver instrumentation using standard laboratory equipment under microcontroller/PC control was constructed and demonstrated. Systematic experiments were conducted on aircraft-grade metallic plates to test the elastic wave generation, reception, and interpretation capabilities of the system. Further investigation is needed to develop automated pulse-echo and acousto-ultrasonic data processing algorithms and to calibrate the system in terms of minimal defect size and locations that can be identified.

The work reported in this paper has shown that unobtrusive permanently attached PZT-wafer active sensors can be used successfully for structural health monitoring of aircraft structures. The advantage of the embedded active sensors method over other health monitoring options is that both near-field and far-field investigation can be achieved with the same active sensor array and instrumentation. For near-field damage detection, the E/M impedance method was used. For far-field damage detection, the pulse-echo ultrasonic method was utilized. Another advantage of our approach is the use of inexpensive non-invasive active sensors instead of the relatively expensive transducers of conventional ultrasonics. These features make this emerging technology a good candidate for large-scale implementation on existing aircraft fleets as well as incorporation in new aircraft constructions.

Acknowledgments

The financial support of Department of Energy through the Sandia National Laboratories, contract doc. No. BF 0133 is thankfully acknowledged. Sandia National Laboratories is a multiprogram laboratory operated by Sandia Corporation, a Lockheed Martin Company, for the United States Department of Energy under contract DE-AC04-94AL85000. The authors are grateful to Elisabeth M. Alford for proofreading and commenting on the manuscript.

References

[1] Giurgiutiu, V., and Zagrai, A., 2002, "Embedded Self-Sensing Piezoelectric Active Sensors for On-Line Structural Identification," ASME J. Vibr. Acoust. **124**, Jan., pp. 116–125.
[2] Bartkowicz, T. J., Kim, H. M., Zimmerman, D. C., and Weaver-Smith, S., 1996, "Autonomous Structural Health Monitoring System: A Demonstration," *Proc., 37th AIAA/ASME/ASCE/AHS/ASC Structures, Structural Dynamics, and Materials Conference*, Salt Lake City, UT, April 15–17.
[3] Boller, C., Biemans, C., Staszewski, W., Worden, K., and Tomlinson, G., 1999, "Structural Damage Monitoring Based on an Actuator-Sensor System," *Proc., SPIE Smart Structures and Integrated Systems Conference*, Newport, CA. March 1–4.
[4] Boller, C., 2001, "Ways and Options for Aircraft Structural Health Monitoring," Smart Mater. Struct., **10**, pp. 432–440.
[5] ANSI/IEEE Std. 176, 1987, *IEEE Standard on Piezoelectricity*, The Institute of Electrical and Electronics Engineers, Inc.
[6] Ikeda, T., 1996, *Fundamentals of Piezoelectricity*, Oxford University Press.
[7] Staveley NDT Technologies, "Sonic Bondmaster™ Product Description," Kennewick, WA 99336.
[8] Cawley, P., 1984, "The Impedance Method for Non-Destructive Inspection," NDT Int., **17**, No. 2, pp. 59–65.
[9] Giurgiutiu, V., and Zagrai, A., 2001, "Electro-Mechanical Impedance Method for Crack Detection in Metallic Plates," *SPIE's 8th Annual International Symposium on Smart Structures and Materials*, March 4–8, Newport Beach, CA, Paper No. 4335–22 (in press).
[10] Lopes, V., Jr., Park, G., Cudney, H., and Inman, D., 1999, "Smart Structures Health Monitoring Using Artificial Neural Network," *2nd International Workshop of Structural Health Monitoring*, Stanford University, September 8–10, pp. 976–985.
[11] Soh, C. K., Tseng, K. K.-H., Bhalla, S., and Gupta, A., 2000, "Performance of Smart Piezoelectric Patches in Health Monitoring of an RC Bridge," Smart Mater. Struct., **9**, Aug., pp. 533–542.
[12] Tseng, K. K.-H., Soh, C. K., and Naidu, A. S. K., 2002, "Non-Parametric Damage Detection and Characterization Using Smart Piezoceramic Material," Smart Mater. Struct. (in press).
[13] Viktorov, I. A., 1967, *Rayleigh and Lamb Waves*, Plenum Press, New York, NY.
[14] Krautkramer, J., and Krautkramer, H., 1990, *Ultrasonic Testing of Materials*, Springer-Verlag.
[15] Rose, J. L., 1999, *Ultrasonic Waves in Solid Media*, Cambridge University Press.
[16] Lemistre, M., Gouyon, R., Kaczmarek, H., and Balageas, D., 1999, "Damage Localization in Composite Plates Using Wavelet Transform Processing on Lamb Wave Signals," *2nd International Workshop of Structural Health Monitoring*, Stanford University, September 8–10, pp. 861–870.
[17] Keilers, C. H., and Chang, F.-K., 1995, "Identifying Delaminations in Composite Beams Using Built-in Piezoelectrics: Part I—Experiments and Analysis; Part II An Identification Method," J. Intell. Mater. Syst. Struct., **6**, Sept., pp. 649–672.
[18] Chang, F.-K., 1998, "Manufacturing and Design of Built-in Diagnostics for Composite Structures," *52nd Meeting of Society for Machinery Failure Prevention Technology*, Virginia Beach, VA, March 30—April 3.
[19] Cawley, P., 1997, "Quick Inspection of Large Structures Using Low Frequency Ultrasound," *Structural Health Monitoring—Current Status and Perspective*, Fu-Kuo Chang, ed., Technomic, Inc.
[20] Blitz, J., Simpson, G., 1996, *Ultrasonic Methods of Non-Destructive Testing*, Chapman & Hall.
[21] Duke, J. C., Jr., 1998, *Acousto-Ultrasonics—Theory and Applications*, Plenum Press.